Numerical simulations of air-assisted primary atomization at different air-to-liquid injection angles

Feichi Zhang[a,*], Thorsten Zirwes[b,c], Simon Wachter[a], Tobias Jakobs[a], Peter Habisreuther[b], Nikolaos Zarzalis[b], Dimosthenis Trimis[b], Thomas Kolb[a], Henning Bockhorn[b], Dieter Stapf[a]

[a]*Institute for Technical Chemistry, Karlsruhe Institute of Technology, Hermann-von-Helmholtz-Platz 1, 76344, Eggenstein-Leopoldshafen, Germany*
[b]*Engler-Bunte-Institute, Division of Combustion Technology, Karlsruhe Institute of Technology, Engler-Bunte-Ring 1, 76131, Karlsruhe, Germany*
[c]*Steinbuch Centre for Computing (SCC), Karlsruhe Institute of Technology, Hermann-von-Helmholtz-Platz 1, 76344, Eggenstein-Leopoldshafen, Germany*

Abstract

Numerical simulations have been performed for a coaxial, twin-fluid nozzle to study the influence of the angle α between the central liquid jet and the annular airflow on the primary atomization process. A glycerol/water mixture with a high dynamic viscosity of 200 mPas is used and the gas-to-liquid ratio is 0.6. The simulations show good agreement with experiments for the breakup morphology. The liquid jet breaks up quickly and its core length L_C decreases with α from 0° to 30°, which is attributable to a reinforced aerodynamic interaction. The flow velocity of the gas phase close to the liquid jet increases with α in this case, which is confirmed by corresponding PIV measurements. This is due to the formation of a high pressure zone at the base of the liquid jet, which results in a favorable pressure gradient in the bulk flow direction. However, further increase of α from 30° to 60° leads to a decreased gas flow velocity along the liquid jet and an increase of L_C. The same behavior has been found for the integral specific kinetic energy k_L in the liquid phase, which represents a measure for the momentum transfer between the gas and liquid phases. k_L increases from $\alpha = 0^\circ$ to 30° and it decreases again with higher α. Moreover,

---

*Feichi Zhang
Email address: `Feichi.Zhang@kit.edu` (Feichi Zhang)

Preprint submitted to International Journal of Multiphase Flow *September 19, 2022*

k_L yields a similar distribution compared with the turbulent kinetic energy (TKE) of a typical turbulent flow in the spectral domain. This is attributed to the local concentration of TKE of the liquid phase in a small region around the tip of the liquid jet. The results reveal that, in addition to the common dimensionless operating parameters, the flow direction has an essential impact on the atomization process. According to the current work, the best atomization performance is achieved at an angle of $\alpha = 30°$. The spectral correlation of k_L with TKE of the gas flow may be used to assess the dynamics of the liquid phase.

Keywords: Primary atomization, Air-assisted atomization, Entrained flow gasification, Hybrid VOF-LES simulation, OpenFOAM

1. Introduction

Entrained flow gasification (EFG) offers the potential to contribute substantially to circular economy and reduction of greenhouse gases as it converts biogenic or fossil based fuels into the chemical building blocks CO and H_2 [1, 2, 3]. For EFG applications, the applied liquid fuels, which typically feature viscosities of up to 1000 mPas and additionally complex rheological behavior, are atomized in the reactor at system pressures of around 80 bar. For atomization into small droplets, gas-assisted atomizers are utilized where the limited amount of oxygen serves as gasification and atomization agent. This dependency leads to a coupling between reaction stoichiometry and gas-to-liquid mass flow ratio (GLR). EFG is typically operating at GLR<1 to ensure the quality of the produced syngas. An optimized atomization of the liquid fuel is of particular importance for the overall performance and the quality of produced syngas in an EFG [4, 5]. Large droplets have to be avoided, as these may lead to incomplete evaporation due to the limited residence time in the gasifier.

There are several studies on the influence of atomization and burner design regarding EFG. To give a brief overview, four recent publications are reviewed in the following. Investigations on the influence of burner operation in an EFG were performed by Risberg and Marklund [6]. Black liquor gasification was performed in 9 experimental cases of varying GLR, system pressure and liquid viscosity, while the near atomizer region was recorded with a high-speed camera. As a main result, ligament-shaped structures increased in concentration for higher viscosity. Spray investigations and the impact on gasification were studied in an atmospheric gasifier by Jakobs et al. [4]. For increasing GLR, a decrease in droplet size was found which led to lower concentration of the formed methane and other organic carbon compounds. First modeling on atmospheric gasification applying the two-phase free jet approach was shown by Hotz et al. [7]. Here, with a given droplet size and atomizer geometry, carbon conversion and the near flame region were studied. The results of the model were in good agreement compared to measurements with OH*-chemiluminescence of the flame at equal conditions in an atmospheric gasifier. Recent research on the influence of burner geometry on atomization was performed by Wu et al. [8], applying an opposed gas-assisted multi-burner during coal-water slurry gasification. Different trends of the resulting droplet size were observed for varying operating conditions. Additionally, particle trajectories and particle fluctuations were measured for varying burner outlet area ratio. Concluding this overview, very heterogeneous studies on atomization and burner design were performed in the past. This leads to the idea of atomization investigation accompanying the gasification process. In order to investigate isolated parameters of the atomizer geometry in this work and complement the literature data, the gas channel angle of gas-assisted atomizers with central liquid jet, as also used in the aforementioned studies, was varied.

Gas-assisted atomization is generally used for liquid fed EFG, where a low-speed liquid stream is subjected to a high-speed gas flow. The liquid jet is disintegrated into small droplets by means of two-phase interactions and momentum transfer between the liquid and gas phases, which leads to shearing forces caused by velocity gradients. The primary breakup of the liquid jet in the near-nozzle region is controlled by a competition between the cohesive and aerodynamic forces, which gives rise to instabilities in the liquid column. Under favorable conditions, the instabilities are amplified and the liquid column disintegrates into ligaments. If the aerodynamic force is high and the primary droplets exceed a critical size, they further break up into smaller droplets, a process known as secondary atomization. The primary breakup, including the initial deformation of the liquid jet core and the disintegration of first liquid fragments, represents an essential step for the entire atomization process, resulting in the formation of the final spray.

Previous experimental works on primary breakup were focused on studying the morphology of the liquid elements by means of high-speed imaging [9, 10, 11, 12, 13, 14, 15, 16, 17, 18, 19]. As different nozzle designs were applied in these works and due to limited optical access into the near-nozzle field, the available data and correlations of breakup properties yield a large scattering. With regard to the breakup morphology, Marmottant and Villermaux [20] showed that the liquid destabilization is initiated by a Kelvin-Helmholtz instability, leading to formation of waves on the liquid core by aerodynamic forces. These surface perturbations grow further due to the Rayleigh-Taylor instability. At the same time, liquid structures protruding from the liquid surface are accelerated through aerodynamic interactions, leading to disintegration of the intact jet core. In [21, 22], the near-field of a canonical two-fluid coaxial atomizer has been studied employing different experimental methods, showing that an increase of the gas-to-fluid momentum ratio M results in a decreased spray angle and a reduced liquid core length. A comprehensive review of the experimental investigation of primary atomization of liquid streams is given in [12], where different atomization regimes according to the operating conditions have been classified. The work further revealed that the geometries and flow field inside the nozzle influence the atomization mechanism and represent the main reason for the experimental discrepancies, which require further investigations to be fully identified and quantified.

In addition to the experimental studies, a large number of simulation works have been performed to study the primary atomization process in the last decades. Among these, direct numerical simulations (DNS) have been performed in [23] for primary atomization of a round liquid water jet injected into high pressure air, where the formation of ligaments has been shown to be triggered by rolling-up the tip of liquid jet through vortices. Srinivasan et al. [24] have imposed oscillatory velocity fluctuations to a round liquid jet inlet issuing into stagnant gas, and the resulting liquid surface destabilization was captured using the volume of fluid (VOF) method. A coupled level set and VOF method (CLSVOF) has been applied in [25] to study the primary breakup of a single cylindrical water jet, showing that liquid turbulent eddies play a dominant role in the development of initial interface instability of the liquid jet. DNS have been conducted for the primary atomization of a planar liquid jet in [26], where different atomization cascades have been classified based on the liquid Reynolds number Re_L and gaseous Weber number We_G. Warncke et al. [27] studied the breakup process of a planar prefilming airblast atomizer with a highly-resolved DNS embedded in a coarse large eddy simulation (LES), which have shown a good agreement with corresponding experiments. In [28], the characteristics of the primary breakup of a liquid jet is analyzed numerically with the VOF method and the influence of varying liquid-gas density, viscosity ratio and injection conditions have been discussed with respect to the required grid resolution. Jiang and Ling [29] have shown via DNS of air-assisted primary atomization that an increase of turbulence intensity at the gas inlet causes enhanced growth of interfacial waves. A review concerning recent progress in modeling primary atomization is given in [30], which outlines the challenges and the numerical methods to address them. In these previous simulation works, the gas-liquid interactions around the intact liquid core have been resolved properly, so that dominant mechanisms prevailing breakup process, such as rupture of the liquid jet core or disintegration of primary liquid ligaments, could be revealed in detail. However, as a wide range of length and time scales governs the liquid-gas interactions and the atomization process is affected by a large number of operational and dimensional parameters, the physics of primary breakup with respect to EFG application has not been unveiled. It is even not sufficient to use solely scalar geometrical and operational parameters such as We_G or Re_L, but the relative direction of the liquid and atomizing fluids may play an important role. This aspect constitutes the objective of the current work.

For that reason, numerical simulations have been conducted in this work for a twin-fluid, coaxial nozzle, which has been designed in the framework of the bioliq® project for EFG of high viscous biomass slurry fuel [2]. The angle between the central liquid jet and the annular gaseous coflow α has been varied from 0° to 60°. Scope of this work is to study the effect of α on the breakup morphology in terms of the liquid core length, whereas the resolved near-field gas and liquid flow dynamics, i.e., flow velocities, pressure and kinetic energies, have been used for justifying the morphological behavior in dependence of α. As the focus of this work is laid on the numerical simulations, the experiments in the current work are used solely to guide the simulations with respect to validation of the observed correlation of breakup morphology in dependence of α and to support findings obtained in the simulations. While the morphological behaviors from measurements and simulations show a good agreement, the simulations further reveal the physical mechanisms behind these phenomena by resolving the multiphase interactions and giving insight into the three-dimensional flow field as well as kinetic energies. Moreover, the simulations provide additional credibility considering a wider range of α beyond the measurement limits.

2. Experimental setups

2.1. Operating conditions

The simulations have been conducted for a generic test rig, which is designed for studying atomization with respect to EFG application under different operating conditions and using different nozzle configurations [5]. It consists of a twin-fluid coaxial nozzle and an optically accessible reactor. For the current study, a glycerol/water mixture (glycerol in wt. 89.5%) is atomized at the temperature of 293 K and pressure of 1 bar. The amount of glycerol is chosen according to the viscosity of pyrolysis oil, which is in a comparable range as the used glycerol/water mixture in this work. The pyrolysis oil serves as fuel for the entrained flow gasifier, where the investigated nozzle system is applied. The mass flow rate of the liquid from the central tube is 20 kg/h and that of the annular air is 12 kg/h, leading to a gas-to-liquid mass flow ratio of $GLR = 0.6$. The relative injection angle α between the central liquid and annular airflow has been varied from $\alpha = 0°$ to $30°$ in the experiment. Figure 1 shows geometries of the used nozzles with different α. The diameters of the liquid and the gas nozzles at the exit plane are kept constant at $d_L = 2$ mm and $d_G = 7.96$ mm. The web thickness connecting the external wall of the liquid tube and inner wall of the gas nozzle is $b = 0.1$ mm.

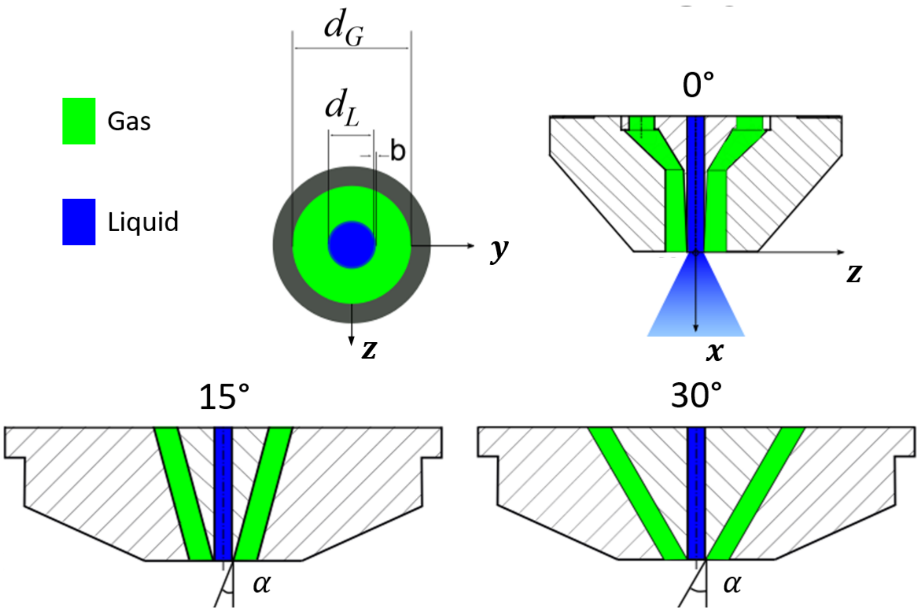

Figure 1: Geometries of the twin-fluid nozzles.

Table 1 summarizes the characteristic dimensionless parameters, with the liquid Reynolds number Re_L, the gas phase Reynolds number Re_G, the momentum ratio MR, the momentum flux ratio M, the aerodynamic Weber number We_{aero} and the Ohnesorge number Oh. The definitions of these non-dimensional parameters are given in Tab.1, where $u_L = 1.45$ m/s and $u_G = 61.36$ m/s are the bulk flow velocities at the exit of the central liquid and annular gas chan-

Table 1: Dimensionless parameters used in this work.

α	$Re_L = \frac{\rho_L u_L d_L}{\mu_L}$	$Re_G = \frac{\rho_G u_G d_{Gap}}{\mu_G}$	$MR = \frac{\rho_G u_G^2 A_G}{\rho_L u_L^2 A_L}$
$0 - 60°$	18	22,600	25.7

α	$M = \frac{\rho_G u_G^2}{\rho_L u_L^2}$	$We_{\text{aero}} = \frac{\rho_G u_R^2 d_L}{\sigma}$	$Oh = \frac{\mu_L}{\sqrt{\rho_L \sigma d_L}}$
$0 - 60°$	1.8	132	0.5

nels of the nozzle, $u_R = u_G - u_L$ the relative velocity between both streams; $d_{Gap} = d_G - d_L - 2b$ is the gap distance of the annulus. The glycerol/water mixture is considered as a Newtonian fluid, which has a dynamic viscosity of $\mu_L = 200$ mPas and a density of $\rho_L = 1223$ kg/m^3. The surface tension of the liquid is $\sigma = 64.2$ mN/m. The viscosity and density of air are equal to $\mu_G = 0.0185$ mPas and $\rho_G = 1.182$ kg/m^3. All these parameters have been kept constant while varying α from 0° to 60°. The readers are referred to [11] for a more details of the nozzle setups.

2.2. Experimental results

Figure 2 shows high-speed images of the primary breakup from the experiments at varying α. The high-speed air flow leads to the formation of liquid instabilities on the liquid column. These instabilities finally result in membranes, as typically observed during the membrane type breakup, reported by Chigier et al.[14] and Lasheras et al. [16, 17]. Those membranes rupture into tiny droplets, while the liquid rim remains intact and subsequently disintegrates via the Rayleigh-Plateau instability into comparably large droplets. These rim structures can also be seen in Fig.2 in the atomizer far field. The breakup morphology remains qualitatively similar with varied α. However, instabilities on the liquid surface appear further upstream with increased α, which can be detected by the earlier onset of wavy structures along the liquid column for $\alpha = 30°$ compared with those for $\alpha = 15°$.

Figure 3 depicts contours of measured time-mean axial velocity $\bar{u}$ obtained from particle image velocimetry (PIV) for the cases with $\alpha = 0°$, $\alpha = 15°$ and

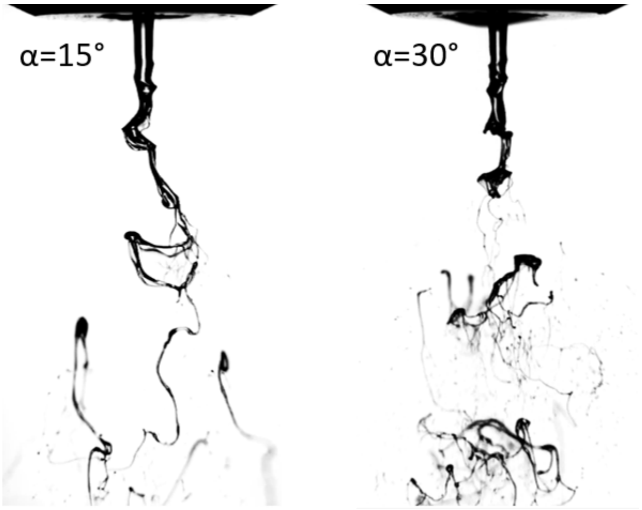

Figure 2: High-speed imaging of primary atomization of coaxial liquid jet at different air-to-liquid injection angles.

$\alpha = 30°$. As the liquid jet reflects the high-intensity laser beam, it is difficult to measure the flow velocity simultaneously with the liquid phase. Therefore, a solid cylindrical pin (blanked fields in Fig.3) with a diameter of 2 mm and a length of 10 mm is mounted at the exit of the central part of the nozzle, which is used to represent the intact liquid core. As a consequence, the velocity field lying in the shadow side of the pin cannot be illuminated by the laser beam and is not measurable. It can be seen from Fig.3 that an increase of α from 0° to 30° results in an increased axial velocity. While the high-speed airflow hits the pin at an increased α, a high pressure zone is formed at the base of the pin. In this case, there is a trade-off between the different components of the velocity vector: the axial velocity at the exit plane of the nozzle decreases with α, whereas the radial velocity component increases with α. The stalling of the flow results in a high pressure zone at the base of the solid pin, where a part of the kinetic energy is transferred to pressure energy. This leads to a favorable pressure gradient in the bulk flow direction and an acceleration of the surrounding gas flow. In the current work, the experiments have been made up to $\alpha = 30°$ according to constructional limitations. It is expected, however, that further increase of α up

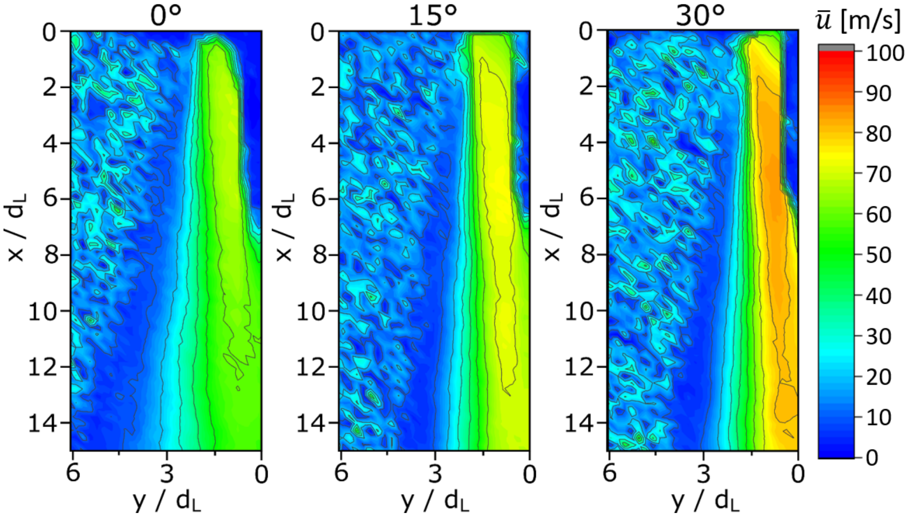

Figure 3: Comparison of contours of time-mean axial flow velocities obtained from PIV measurements for $\alpha = 0°$, $\alpha = 15°$ and $\alpha = 30°$.

to a range of $\alpha > 45°$ will lead to a significant decrease of the axial velocity of the gas flow, which cannot be balanced out by the favorable pressure gradient caused by the high pressure zone at the jet root. This behavior has been confirmed in the following by the numerical simulations (see Fig.8 and Fig.9). Further results from the experiments can be found in [9], where the increased axial flow velocity with α has been shown to result in a decrease of the SMD (Sauter Mean Diameter), confirming an improved atomization performance with increased α.

3. Simulation setups

3.1. Computational grid and boundary conditions

Figure 4 depicts a cutting plane of the 3D computational domain passing through the centerline axis, where $d_L = 2$ mm is the diameter of the central liquid nozzle at the exit plane. The cone-shaped domain starts from the nozzle exit plane and it covers the range of primary atomization. It has a length of $30d_L$ in bulk flow direction, with the diameters of $10d_L$ and $20d_L$ at the nozzle exit plane and at the outlet of the domain, as indicated in Fig.4. The

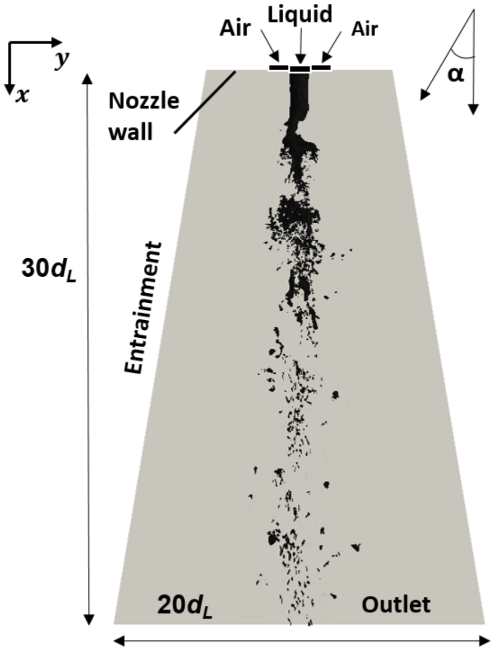

Figure 4: Computational domain used for the simulation.

internal geometry of the nozzle was not considered in order to use the same computational grid while varying α. This allows a systematic evaluation of the effect of α on the atomization process, excluding the influence of nozzle interior designs. The dimensions of the domain have been selected based on a compromise between simulation accuracy and computational cost. It allows use of refined grids in the near-nozzle field and the outlet plane lies sufficiently far away from the jet core, allowing zero gradient type boundary conditions at the outlet. x indicates the axial direction and the origin is set at the center of the liquid inlet.

The top left part of Fig.5 illustrates the boundary conditions used at nozzle exit plane ($x/d = 0$). As the inlet conditions may have a significant impact on breakup of the liquid jet, the computational domain has been deliberately selected excluding the nozzle interior geometry and only top-hat velocity profiles are used for both gas and liquid inlets. These allow a targeted assessment of

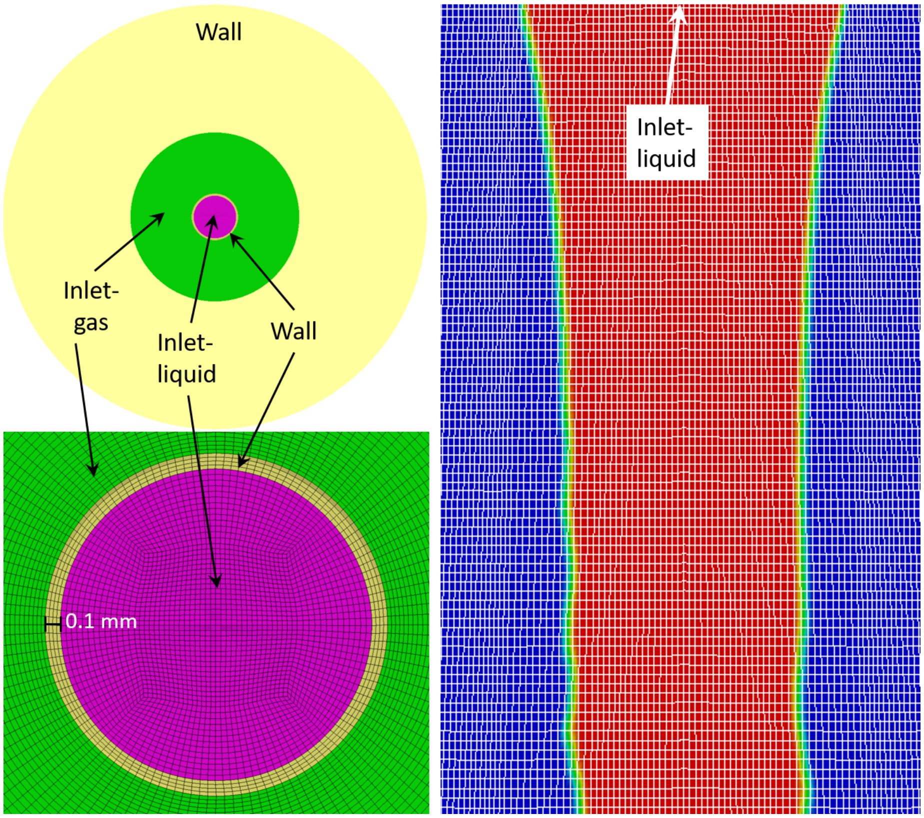

Figure 5: Boundary conditions and surface mesh at the nozzle exit plane (left); contours of liquid volume fraction along with computational grid on a cutting plane passing through the centerline axis (right).

the effect of α, which has been varied from $\alpha = 0^\circ$ to 60° in this work. No-slip condition is used for the walls at the nozzle orifice, i.e., the ring wall bridging the liquid and gas channels as well as the external wall of the annular gas channel. The temperature is prescribed at 293 K for both gas and liquid inlets. $f = 0$ is used for the gas inlet and $f = 1$ at the liquid inlet. The entrainment boundary allows ambient air to enter into the domain from the sides. At the entrainment and outlet boundaries, gradients of the transport variables are set to zero.

The lower left part of Fig.5 depicts the grid distribution at the nozzle exit plane, which illustrates the mesh topology given by a O-type grid. The right part of Fig.5 shows a meridian cutting-plane through the computational grid, along with contours of instantaneous liquid volume fraction f. It can be seen that the gas-liquid interface of the intact liquid jet represented by the sharp gradient of f has been resolved by approx. 3-4 cells. The computational grid consists of 9.5 million hexahedral elements, which are locally refined close to the liquid jet. It has a smallest size of $\Delta_{\mathrm{min,r}} = 25$ μm in the radial direction and the smallest grid length in the axial direction is $\Delta_{\mathrm{min,r}} = 50$ μm. The grid size expands with a constant small factor in the radial and axial directions. The diameter of the central liquid nozzle has been resolved with 60 computational cells and the gap of the annular gas channel with 50 cells. The grid resolution is chosen according to the previous work [31], where a grid independence study has been performed for the same nozzle system at $\alpha = 0°$. It has been shown there that further refining the grid will not lead to a discernible change in terms of the breakup morphology, but more small-scale liquid fragments further downstream are resolved. Note that the focus of this work is to study the primary breakup processes of the liquid core, along with disintegration of large-scale liquid ligaments. The current resolution is not sufficient to resolve small-scale droplets generated by the secondary atomization.

3.2. Numerical setups

OpenFOAM-v2006 has been used to simulate the turbulent two-phase flow. The gas-liquid interface is captured employing the volume of fluid (VOF) method [32], which solves a balance equation for the liquid volume fraction f

$$\partial_t f + \nabla \cdot (\tilde{\mathbf{v}} f) = \nabla \cdot (f\,(1-f)\,\tilde{\mathbf{v}}_r) \tag{1}$$

The relative velocity $\mathbf{v}_r$ in Eq.(1) is modeled by

$$\mathbf{v}_r = \mathbf{v}_L - \mathbf{v}_G = |\mathbf{v}|\ \mathbf{n} = |\mathbf{v}|\ \frac{\nabla f}{|\nabla f|} \tag{2}$$

where $\mathbf{n}$ is the surface normal unit vector. $f = 1$ indicates the pure liquid phase and $f = 0$ the pure gas phase. The intermediate values of $0 < f < 1$ identify the gas-liquid interface. The VOF method represents a state-of-the-art technique for modeling multiphase flows and has been extensively used in previous works [24, 23, 25, 33, 31, 28]. The solved equations in OpenFOAM for VOF are provided in more detail in [33, 31] and the elaborated theory behind the method can be found in [34].

The balance equations are solved in a fully compressible formulation, along with 2nd order interpolation schemes for discretizations of the convective and diffusive terms. The time step is set to 0.2 μs, which leads to a maximum CFL (Courant–Friedrichs–Lewy) number of 0.5. For all simulation cases, initial fields of the liquid volume fraction and the flow velocity are set to 0 for the whole computational domain. Liquid and gas flows enter the domain at the same time at $t = 0$, which develop over time to a quasi-stationary state. From that point on, statistical averaging has been performed to obtain the time mean and rms values of the flow variables for a physical time of 80 ms or 400,000 time steps, which corresponds to more than 10 flow-through times based on the bulk velocity of the liquid stream and the primary breakup length. The turbulent flow is modeled in this work with the large eddy simulation (LES) technique, which resolves the large-scale flow structures down to the cut-off scale. The wall-adapted local eddy viscosity (WALE) model [35] is applied for modeling the sub-grid scale Reynolds stresses, which accounts for the unresolved turbulent fluctuations.

Note that the experiments were made up to $\alpha = 30^\circ$ due to limitations given by the nozzle manufacturing. Moreover, a solid pin is used in the PIV experiment for representing the liquid jet, as the state-of-the-art PIV technique does not allow a simultaneous measurement of the gas flow together with the liquid jet. Therefore, a comprehensive comparison between the experiment and the simulation, including all that flow velocities, breakup morphology, liquid core length and pulsating frequency, is not feasible and beyond the scope of the current work, which focuses on studying the effect of α by means of numerical simulations. In this context, the experiment is used to guide the simulations in confirming the observed qualitative behavior with regard to the impact of α on the breakup morphology and the gaseous flow velocity. On the other hand, as the experiment is limited by optical access, the physical causes of these phenomena have been revealed in more detail by resolving the multiphase flows in the simulations.

4. Simulation results

4.1. Breakup mechanism

In Fig.6, volume-rendered views of instantaneous f are used to visualize the liquid jet core. In agreement with experimental results obtained from high speed imaging shown in Fig.2, the simulations reveal a pulsating-mode breakup of the liquid jet, along with disintegration of membrane-type ligaments. The shear layer between the high-speed annular airflow and low-speed liquid jet results in aerodynamic forces acting on the liquid jet and onset of initial flow instabilities with wavy structures along the jet surface, which is triggered by the Kelvin-Helmholtz instability.

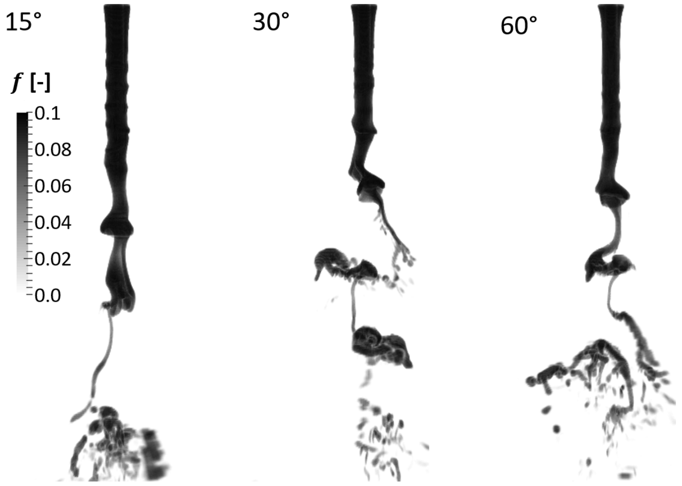

Figure 6: Volume rendering of liquid volume fraction calculated from VOF-LES simulations of primary breakup of coaxial glycerol/water jet at different air-to-liquid injection angles.

Figure 7 shows contours of instantaneous velocity in the main flow direction on a meridian cutting-plane, where the liquid jet core is indicated by the iso-contour of $f = 0.5$. The liquid column is contracted with increasing α, which results in a reduced diameter of the core jet. At the tip of the liquid jet, large-scale, concentric vortices are generated, which can be detected from the recirculation zone near the tip of the liquid jet. These vortices penetrate into the liquid jet from the side, so that the growth of the jet is inhibited. At the same time, the tip of the liquid jet is strained toward downstream direction and yields a tumbling motion around the centerline axis, until first liquid ligaments pinch off from the tip. The breakup mechanism is representative for all cases with different α. The axial flow velocity increases with α from 15° to 30° and it decreases again by further increasing α from 30° to 60°.

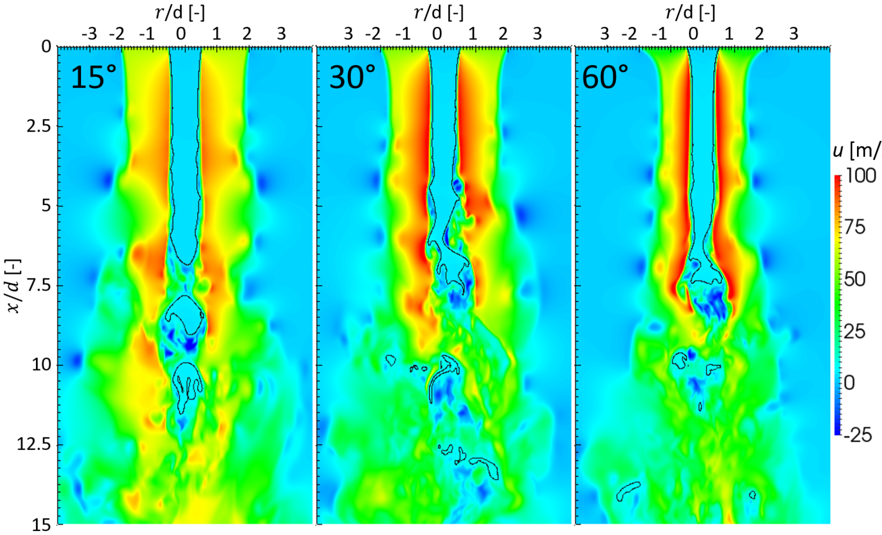

Figure 7: Contours of instantaneous axial velocity during primary breakup of coaxial liquid jets at different air-to-liquid injection angles.

The same behavior can be detected from contours of the time-averaged axial velocity $\bar{u}$ shown in Fig.8 on the left, where the liquid jet core is depicted by the iso-surface of the time-mean liquid volume fraction at $\bar{f} = 0.5$. The increase of $\bar{u}$ results in a reinforced aerodynamic force exerted upon the liquid jet, which leads to an enhanced momentum transfer from the gas to the liquid phase. Therefore, the jet disintegrates faster and the length of the liquid jet core L_C, determined with the largest axial distance of the $\bar{f} = 0.5$ iso-surface, decreases with α until

30°. The increase of $\bar{u}$ from $\alpha = 0°$ to 30° has been confirmed both by the PIV measurements (see Fig.3) and the numerical simulations (see also Fig.8 on the right).

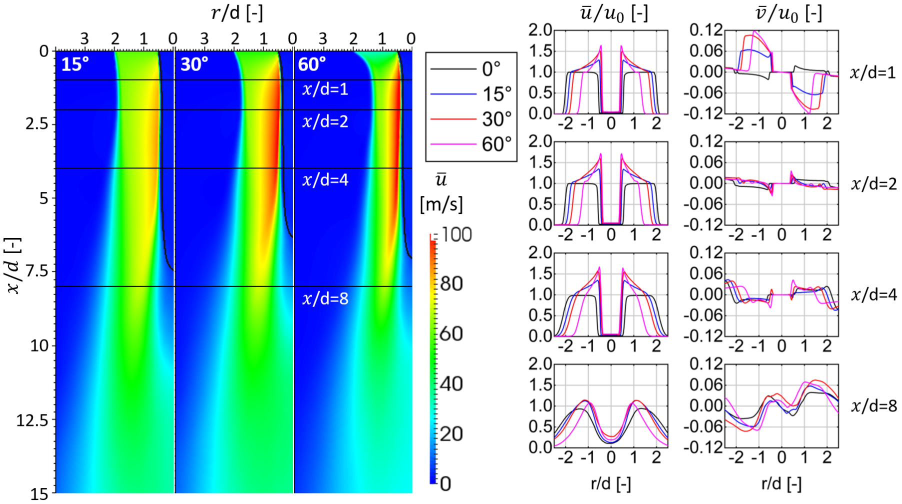

Figure 8: Comparison of contours of time-mean axial velocity (left) and radial profiles of time-mean streamwise and radial flow velocities (right) at different air-to-liquid injection angles.

Figure 8 on the right depicts radial profiles of the time-mean streamwise and radial velocities at different axial positions, which are indicated in Fig.8 on the left by the horizontal solid lines. $\bar{u}$ is large in the range of the annular gas stream and it decreases steeply at the liquid jet surface with $|r/d| \approx 0.5$. $\bar{u}$ is small for large r/d due to entrainment of ambient gas. In the near-nozzle region with $x/d \leq 6$, although the maximum value of $\bar{u}$ increases strictly with α, the surface area below the $\bar{u}$ profiles is clearly decreased while increasing α from 30° to 60°. This results in a decreased axial momentum of the gas phase and an attenuated multiphase momentum exchange, leading to a decrease of L_C.

As the high-speed airflow hits the liquid column at an inclined angle, the gas flow velocity at the base of the liquid jet decreases to adapt to the low-speed liquid jet. In particular, the radial motion of the gas is forced to be stalled

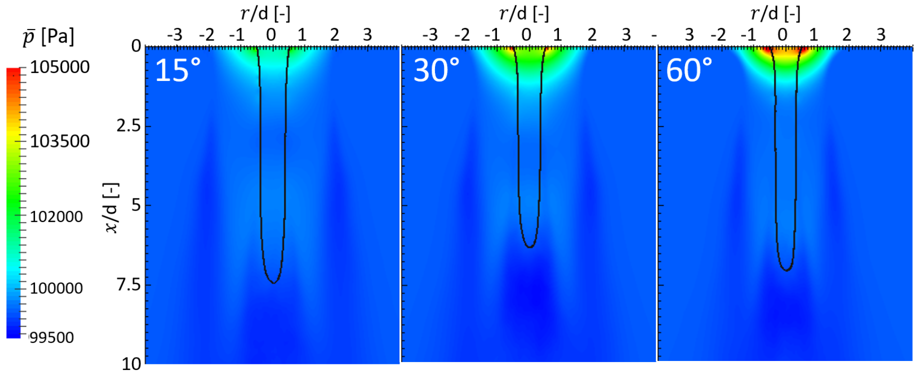

Figure 9: Contours of time-mean static pressure calculated from VOF-LES of primary breakup of coaxial liquid jets at different α.

at the surface of the liquid jet. This behavior is shown in Fig.8 on the right by the profiles of $\bar{v}$, whose magnitude steeply decreases to zero in the range of $|r/d| \leq 0.5$ at $x/d = 1$. At the same time, the diameter of the liquid jet decreases continuously with α, leading to a narrowing of the velocity profiles shown in Fig.8 on the right. Therefore, one part of the kinetic energy from the radial momentum of the airflow is converted directly to pressure energy while hitting the liquid jet at $\alpha > 0$. This generates a high pressure zone at the base of the liquid jet, as shown in Fig.9 by contours of the time-mean static pressure $\bar{p}$, with the liquid jet core depicted by iso-contours of $\bar{f} = 0.5$. The pressure near the base of the liquid jet increases strictly with α, which results in a favorable pressure gradient and an acceleration of the airflow towards the main flow direction. This explains the increase of gas flow velocity with α for $\alpha \leq 30°$.

However, increasing α from 30° to 60° does not result in a higher $\bar{u}$ around the liquid jet and L_C increases (see Fig.8). This is attributed to the considerably decreased axial momentum of the gas flow at $\alpha = 60°$, which cannot be compensated by the higher static pressure at the base of the liquid jet. As shown in Fig.8 on the left, the effective area below the profile of $\bar{u}$, which indicates a measure of the axial momentum in the gas phase, is decreased for $\alpha = 60°$ compared with that for $\alpha = 30°$. In this case, a major part of the kinetic energy within the gas phase has been spent to constrict the liquid column, instead of to create shear forces along the liquid jet. Although not shown here, similar behavior has been found for the root-mean-square (rms) values of the velocity fluctuations close to the liquid jet, which increase from $\alpha = 0°$ to $30°$ and decreases again with further increased α. The results confirm that the atomization process is controlled by the nature of the turbulent gas flow.

4.2. Breakup Length

Figure 10 shows profiles of the time-mean (solid lines for $\bar{f}$) and rms values (dashed lines for f') of f along the centerline axis. Throughout the breakup process, $\bar{f}$ decreases rapidly at the location of breakup length $x = L_C/d_L$ from 1 (liquid) to 0 (gas). In the range of $0 \leq \alpha \leq 30°$, $\bar{f}$ starts to decrease at smaller x/d_L position, confirming a reduction of L_C with α. However, in the simulations $\bar{f}$ starts to decrease at larger x/d_L with further increased α from $30°$ to $60°$, leading to an increase of L_C. The behavior of L_C vs. α can also be perceived in Fig.9 by means of contours of $\bar{f} = 0.5$ as well as from the profiles of f' in Fig.10, where the maximum value of f' with $f'_{\max} \approx 0.5$ shifts with α.

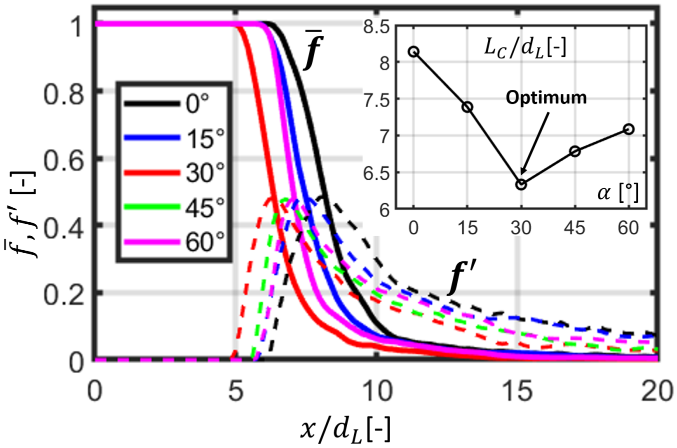

Figure 10: Profiles of time-mean and rms values of liquid volume fraction along the centerline axis for different α.

The location of $f'_{\max} \approx 0.5$ (corresponding to $\bar{f} \approx 0.5$) has been used to determine L_C quantitatively from the simulations [31], which is shown in Fig.10 against α in the upper right subplot. The predicted L_C decreases from $\alpha = 0°$ to $\alpha = 30°$ and it increases again from $\alpha = 30°$ to $\alpha = 60°$. The results reveal that using only scalar operating parameters like Re or We is not sufficient for an accurate description of the atomization process and, the vector property considering direction of the flow velocity has an essential impact on the atomization process. The current simulation result indicates a most effective atomization in the range of $30° < \alpha < 45°$.

4.3. Two-Phase Momentum Transfer

The breakup of the liquid jet is triggered by two-phase momentum transfer in terms of aerodynamic forces exerted by the high-speed gas flow on the low-speed liquid jet, which increases the kinetic energy in the liquid phase and causes stretching of liquid surface. The liquid jet breaks up, when the aerodynamic force overcomes the resistant cohesive, surface tension force of the liquid. In order to assess quantitatively the breakup efficiency, the kinetic energy density of the liquid phase has been evaluated by integration of the volume-specific kinetic energy of the liquid k_f

$$k_f = f \cdot \frac{1}{2}\,\rho_L \mathbf{v}_L^2 \quad \text{in} \quad [\mathrm{J/m^3}] \tag{3}$$

over the whole computational domain

$$k_L = \frac{K_L}{V_L} = \frac{\int_V k_f \,\mathrm{d}V}{\int_V f \,\mathrm{d}V} \quad \text{in} \quad [\mathrm{J/m_L^3}] \tag{4}$$

The velocity of the liquid phase $\mathbf{v}_L$ is evaluated by

$$\mathbf{v}_L = \mathbf{v} + (1 - f)\,\mathbf{v}_r \tag{5}$$

with $\mathbf{v}$ being calculated from the balance equation of momentum and $\mathbf{v}_r$ given in Eq.(2) [31]. K_L and V_L are the total kinetic energy and volume of the liquid phase. k_f represents liquid phase kinetic energy averaged locally with regard to the cell volume, whereas k_L denotes an integral quantity measuring the attained kinetic energy per unit liquid volume. Both k_f and k_L fluctuate over time due to the unsteady nature of the breakup process. As the specific kinetic energy of the liquid stream at the nozzle exit is constant for all cases, i.e., $k_{L,0} = \rho_L u_L^2/2$, an increase of k_L denotes specifically a reinforced momentum transfer from the gas to the liquid phase.

Figure 11 on the left depicts time-mean k_L as a function of time-mean V_L, where $\bar{V}_L$ represents a measure of L_C. $\bar{k}_L$ increases with α from 0° to 30° and it yields a negative correlation with V_L in the range of $\alpha \leq 30°$, which is in agreement with the behavior of an increase of gas flow velocity and a decrease of L_C with α. The reversed trend is found for further increased α from 30° to 60°, where $\bar{k}_L$ decreases with α. Even though the resolved liquid volumes $\bar{V}_L$ are almost identical for $\alpha = 30°$ and 60°, $\bar{k}_L$ at $\alpha = 30°$ (red point in Fig.11) is considerably larger compared with that for $\alpha = 60°$ (magenta point in Fig.11). The result confirms an optimal injection angle at approximately $\alpha = 30°$ for best atomization performance, which is attributed to the most effective interphase momentum exchange.

The dynamics of a common turbulent flow is given by fluctuations of its kinetic energy over a wide range of length and time scales, which yields a cascade-like distribution in the wave-length or spectral domain [36]. In order to accessthe mechanism of the momentum transfer from the turbulent gas flow to the liquid phase over the broadband scales in more detail, spectral densities E_{k_L} have been evaluated from Fourier transformation of time series of k_L and are shown in Fig.11 on the right. E_{k_L} exhibits a similar trend in the frequency domain for different α, which is largest in the low frequency range ($f < 100$ Hz) and it decreases with f in a quasi-linear way in a double-logarithmic scaling in the high frequency range ($f > 200$ Hz). As indicated in Fig.11 by the dashed line, the decrease of k_L in the spectral domain follows exclusively $E_{k_L} \propto f^{-5/3}$, which corresponds to the decay rate of turbulent kinetic energy (TKE) in the inertial sub-range for a general turbulent flow. The dissipation range is not visible in Fig.11, as the smallest length scale of the turbulent flow is not resolved on the current computational grid.

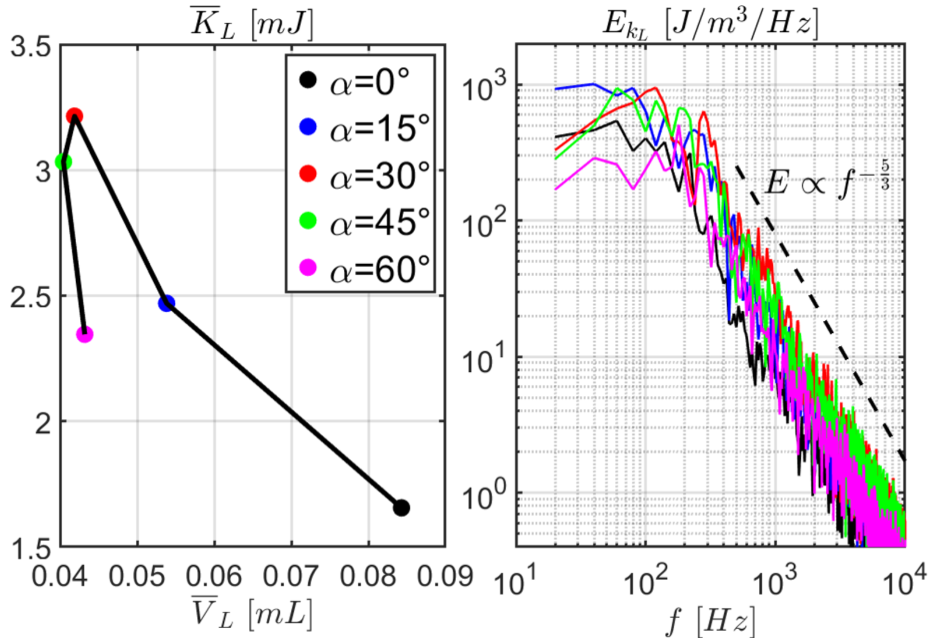

Figure 11: Time-averaged specific liquid phase kinetic energy vs. time-mean liquid volume (left) and spectra of kinetic energy density of the liquid phase (right).

Although k_L represents an integral quantity evaluated from volume integration of k_f (see Eq.(4) and Eq.(3)), it reproduces a self-similar distribution for E_{k_L} for different α cases. The reason is identified in Fig.12 by means of contours of TKE of the liquid phase

$$k_{\text{turb}} = \frac{1}{2}\bar{f}\rho_L\overline{\mathbf{v}'^2} = \frac{1}{2}\bar{f}\rho_L\overline{(\mathbf{v}-\overline{\mathbf{v}})^2} \quad \text{in} \quad [\text{J}/\text{m}_\text{L}^3] \tag{6}$$

with $\mathbf{v}'$ being the temporal fluctuations of flow velocity in the liquid phase. It is noticeable that the largest values of k_{turb} or the strongest fluctuations of the liquid phase kinetic energy is concentrated in a small region downstream the tip of the liquid jet (in a distance of approx. 10-15% of L_C). As shown in Fig.7, this location is dominated by a reinforced interaction of the liquid jet with coherent vortices from the gas flow, where primary large-scale ligaments disintegrate from the liquid jet. Therefore, the strongest fluctuations of f between 1 (pure liquid state) and 0 (pure air state) is found there (see also Fig.10), which leads to large

k_{turb}. The behavior with concentrated high k_{turb} around the jet tip gives rise to the strong similarity between E_{k_L} with that of a common turbulent gas flow, as shown in Fig.11 on the right.

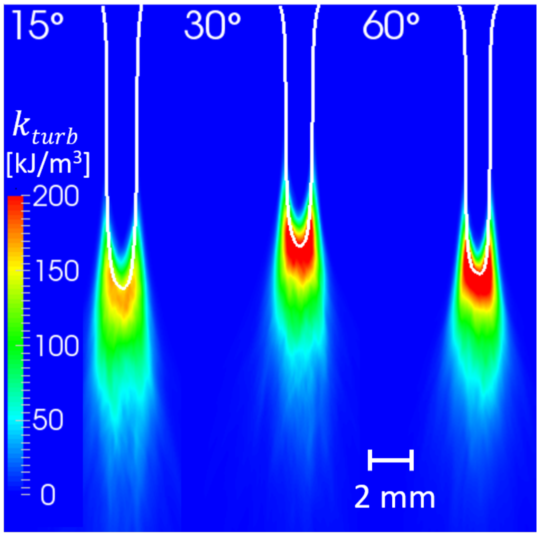

Figure 12: Contours of turbulent kinetic energy in the liquid phase. The white solid lines indicate the intact jet core identified by $\bar{f} = 0.5$.

The strong correlation between kinetic energy spectra of the gas and liquid flows reveals that the cascade-like properties of the turbulent gas flow is transferred conservatively to the liquid phase. The behavior has been confirmed for all simulated cases with different α, as shown in Fig.11 on the right. In addition, the magnitude of E_{k_L} increases with α up to $\alpha = 30^\circ$ and it decreases again beyond that, which is valid almost for the whole frequency range. The result is in agreement with that obtained for $\bar{k}_L$ shown in Fig.11 on the left and corresponds to the correlations of streamwise velocity and liquid core length in dependence of α. The spectral correlation of TKE from the liquid and gas phases may be used to assess the energy budget or dynamics of the liquid phase. For that purpose, a transfer function could be developed for estimation of the energy spectra within the liquid phase from those of the gas phase.

4.4. Discussions

In summary, inclination of the coflow air results in a high pressure zone at the root of liquid jet, which accelerates the gas flow around the liquid column. The increased gas flow velocity leads to a locally enhanced momentum flux ratio and turbulent fluctuations in the gas flow in the range of $\alpha \leq 30^\circ$. Consequently, the momentum transfer or the aerodynamic force exerted by the gas flow on the liquid jet is stronger, leading to an increase of the energy budget in the liquid phase, as shown in Fig.11. The reversed trend is found for further increase of α from 30° to 60°. In this case, the loss of gaseous axial momentum due to inclination of the annular airflow cannot be compensated by the favorable pressure gradient generated by the high pressure zone at the base of the liquid column, leading to an attenuated turbulent fluctuations in both gas and liquid phases. Therefore, the liquid jet breaks up faster or L_C decreases from $\alpha = 0^\circ$ to 30° and vice versa for varying α from 30° to 60°.

The result is comparable with that from DNS of an air-assisted atomization shown in [29], where an increase of turbulence intensity at the gas inlet has strengthened the growth of interfacial instabilities and breakup of the liquid jet. In the current work, the gas phase turbulent intensity is modified in terms of the inclination angle through the mechanism discussed above. Similar behavior has been shown by numerical simulations of planar air-blast atomization in [37], where an increase of the inclination angle between the gas and liquid inflows from 0° to 30° has led to an enhanced primary atomization. Whereas a planar liquid sheet is used and α has been varied up to 30° in [37], a round liquid jet from a co-axial air-assisted setup is used in this work and α has been varied till 60°.

As shown in Fig.10, the liquid core remains intact for around $10d_L$ due to the small M used in this work (see Tab.1). For large M with $M > 10$, L_C can be significantly shorter with a few d_L. However, the basic mechanism, given by a stalling airflow at root of the liquid jet and a narrowing of the liquid column due to an inclination of the air-to-liquid angle, is unchanged for large M. Therefore, the observed phenomenon of an increased axial momentum or decreased L_C from $\alpha = 0°$ to $\alpha = 30°$ and vice versa for varying α from 30° to 60°, is valid for large M, too. However, the effect of α could be weaker at large M, because the contributions of M may dominate the influence of α. In fact, α should be regarded as a general influencing parameter with an equivalent effect similar to other operational or dimensional parameters such as M, We_G, Re_L or the wall thickness connecting the gas and liquid nozzles. All these parameters together determine the final atomization characteristics. If one of them is excessively large, e.g. M, the role or effectiveness of other parameters could be subordinate.

Despite the fact that the simulation and experimental results have revealed the same morphological change of the liquid jet as well as the trend for the near-field velocity in dependence of α, the numerical setups such as the grid resolution or the boundary condition may have a significant impact on the results. For instance, according to our previous experience [31], a refined grid will lead to an improved resolution of small-scale liquid fragments, the morphology of the main liquid jet can however be reproduced well with a relatively coarse grid. In addition, as the exact inflow conditions at the nozzle exits are unknown from the experiment, top-hat velocity profiles are used in this work at both liquid and gas inlets, which remain constant for all cases with different α. Although this represents a strong simplification compared with the experiment, it allows a systematic evaluation specifically for the effect of α. In this way, the inconsistencies or uncertainties caused by the internal nozzle designs, the turbulent flow conditions or developments of boundary layers within nozzles, which have a strong influence on the breakup of the liquid jet, are excluded.

5. Conclusions

Highly-resolved numerical simulations have been carried out to study the effect of varied air-to-liquid jet angles α on the primary atomization using coaxial, air-assisted nozzles. The simulation results have shown good agreement with corresponding experiments for the breakup morphology. An increase of α from

$0°$ to $30°$ leads to a shorter liquid core length L_C, which is attributed to the increased gas flow velocity along the liquid jet. The same behavior of increased flow velocity and decreased L_C with α up to $30°$ has been confirmed by PIV experiments. However, the reversed effect has been found for further increased α from $30°$ to $60°$ in the numerical simulations. The same behavior has been found for the kinetic energy within the liquid phase, which increases with α from $0°$ to $30°$ and decreases again with α. Therefore, there exists an optimal air-to-liquid injection angle in the range of $30° < \alpha < 45°$ for best atomization performance for co-axial, air-assisted nozzle.

For all cases, the spectra of the total turbulent kinetic energy (TKE) of the liquid exhibit a self-similar shape, which compares well with the usual TKE spectrum. This gives rise to the dynamic mechanism during the broadband multiphase momentum exchange and points out that the bulk liquid phase TKE is concentrated within a small region locally dominated by the strongest gas-liquid interactions. The behaviour has been justified by means of the distributions of TKE in the liquid phase.

In conclusion, the relative injection angle between the liquid and air flows has an essential impact on the atomization process, which has to be taken into account in addition to the general scalar operating parameters such as Re or We. For the current nozzle setup and operating conditions, an optimal atomization performance is achieved at $\alpha = 30°$. The spectral correlations between turbulent kinetic energy in the liquid and gas phases may be used to model the dynamic behavior of disintegrated liquid ligaments, for instance, through a momentum transfer function from the gas to the liquid phase, which could be further processed to derive dynamic characteristics of the final spray.

Acknowledgments

The authors gratefully acknowledge the financial support by the Helmholtz Association of German Research Centers (HGF), within the research field MTET (Materials and Technologies for the Energy Transition), subtopic “Anthropogenic

Carbon Cycle" (38.05.01). This work utilized computing resources provided by the High Performance Computing Center Stuttgart (HLRS) and the Steinbuch Centre for Computing (SCC) at the Karlsruhe Institute of Technology. The work leading to this publication was supported by the PRIME programme of the German Academic Exchange Service (DAAD) with funds from the German Federal Ministry of Education and Research (BMBF).

References

[1] C. Higman, M. Burgt, Gasification., Gulf Professional Publishing, USA, 2008.

[2] T. Kolb, M. Aigner, R. Kneer, M. Mueller, R. Weber, N. Djordjevic, Tackling the challenges in modelling entrained-flow gasification of low-grade feedstock, J. Energy Inst. 89 (4) (2016) 485–503.

[3] K. Svoboda, M. Pohořelỳ, M. Hartman, J. Martinec, Pretreatment and feeding of biomass for pressurized entrained flow gasification, Fuel Process. Technol. 90 (5) (2009) 629–635.

[4] T. Jakobs, N. Djordjevic, S. Fleck, M. Mancini, R. Weber, T. Kolb, Gasification of high viscous slurry r&d on atomization and numerical simulation, Appl. Energy 93 (2012) 449–456.

[5] S. Wachter, T. Jakobs, T. Kolb, Experimental investigation on the influence of system pressure on resulting spray quality and jet breakup applying pressure adapted twin-fluid nozzles, Int. J. Multiph. Flow 125 (2020) 103189.

[6] M. Risberg, M. M., Visualizations of gas-assisted atomization of black liquor and syrup/water mixtures at eleveated ambient pressures, At. Sprays 19(10) (2009).

[7] C. Hotz, M. Haas, S. Wachter, S. Fleck, T. Kolb, Two-phase free jet model of an atmospheric entrained flow gasifier, Fuel 304 (2021) 121392.

[8] X. Wu, Q. Guo, Y. Gong, J. Liu, X. Luo, T. Wu, G. Yu, Influence of burner geometry on atomization of coal water slurry in an entrained-flow gasifier, Chemical Engineering Science 247 (2022) 117088.

[9] S. Wachter, T. Jakobs, T. Kolb, Comparison of central jet and annular sheet atomizers at identical gas momentum flows, Ind. Eng. Chem. Res. 60 (30) (2021) 11502–11512.

[10] S. Wachter, T. Jakobs, T. Kolb, Effect of solid particles on droplet size applying the time-shift method for spray investigation, Appl. Sci. 10 (21) (2020) 7615.

[11] S. Wachter, T. Jakobs, T. Kolb, Effect of gas jet angle on primary breakup and droplet size applying coaxial gas-assisted atomizers, in: International Conference on Liquid Atomization and Spray Systems (ICLASS), Vol. 1, 2021, p. 31.

[12] C. Dumouchel, On the experimental investigation on primary atomization of liquid streams, Exp. Fluids 45 (3) (2008) 371–422.

[13] H. Eroglu, N. Chigier, Z. Farago, Coaxial atomizer liquid intact lengths, Phys. Fluids A: Fluid Dyn. 3 (2) (1991) 303–308.

[14] N. Chigier, Z. Farago, Morphological classification of disintegration of round liquid jets in a coaxial air stream, At. Sprays 2 (2) (1992) 137–153.

[15] C. Engelbert, Y. Hardalupas, J. H. Whitelaw, Breakup phenomena in coaxial airblast atomizers, Proc. R. Soc. A: Math. Phys. Eng. Sci. 451 (1941) (1995) 189–229.

[16] J. Lasheras, E. Villermaux, E. Hopfinger, Break-up and atomization of a round water jet by a high-speed annular air jet, J. Fluid Mech. 357 (1998) 351–379.

[17] J. C. Lasheras, E. Hopfinger, Liquid jet instability and atomization in a coaxial gas stream, Annu. Rev. Fluid Mech. 32 (1) (2000) 275–308.

[18] U. Shavit, Gas-liquid interaction in the liquid breakup region of twin-fluid atomization, Exp. Fluids 31 (5) (2001) 550–557.

[19] W. Mayer, R. Branam, Atomization characteristics on the surface of a round liquid jet, Exp. Fluids 36 (4) (2004) 528–539.

[20] P. Marmottant, E. Villermaux, On spray formation, J. Fluid Mech. 498 (2004) 73–111.

[21] N. Machicoane, G. Ricard, R. Osuna-Orozco, P. D. Huck, A. Aliseda, Influence of steady and oscillating swirl on the near-field spray characteristics in a two-fluid coaxial atomizer, Int. J. Multiph. Flow 129 (2020) 103318.

[22] J. K. Bothell, N. Machicoane, D. Li, T. B. Morgan, A. Aliseda, A. L. Kastengren, T. J. Heindel, Comparison of x-ray and optical measurements in the near-field of an optically dense coaxial air-assisted atomizer, Int. J. Multiph. Flow 125 (2020) 103219.

[23] J. Shinjo, A. Umemura, Simulation of liquid jet primary breakup: Dynamics of ligament and droplet formation, Int. J. Multiph. Flow 36 (7) (2010) 513–532.

[24] V. Srinivasan, A. J. Salazar, K. Saito, Modeling the disintegration of modulated liquid jets using volume-of-fluid (vof) methodology, Appl. Math. Model. 35 (8) (2011) 3710–3730.

[25] F. Xiao, M. Dianat, J. J. McGuirk, Les of turbulent liquid jet primary breakup in turbulent coaxial air flow, Int. J. Multiph. Flow 60 (2014) 103–118.

[26] A. Zandian, W. Sirignano, F. Hussain, Planar liquid jet: Early deformation and atomization cascades, Phys. Fluids 29 (6) (2017) 062109.

[27] K. Warncke, S. Gepperth, B. Sauer, A. Sadiki, J. Janicka, R. Koch, H.-J. Bauer, Experimental and numerical investigation of the primary breakup of an airblasted liquid sheet, Int. J. Multiph. Flow 91 (2017) 208–224.

[28] H. Grosshans, A. Movaghar, L. Cao, M. Oevermann, R.-Z. Szász, L. Fuchs, Sensitivity of vof simulations of the liquid jet breakup to physical and numerical parameters, Comput. Fluids 136 (2016) 312–323.

[29] D. Jiang, Y. Ling, Impact of inlet gas turbulence on the formation, development and breakup of interfacial waves in a two-phase mixing layer, J. Fluid Mech. 921 (2021).

[30] M. Gorokhovski, M. Herrmann, Modeling primary atomization, Annu. Rev. Fluid Mech. 40 (2008) 343–366.

[31] F. Zhang, T. Zirwes, T. Müller, S. Wachter, T. Jakobs, P. Habisreuther, N. Zarzalis, D. Trimis, T. Kolb, Effect of elevated pressure on air-assisted primary atomization of coaxial liquid jets: Basic research for entrained flow gasification, Renew. Sustain. Energy Rev. 134 (2020) 110411.

[32] A. Prosperetti, G. Tryggvason, Computational methods for multiphase flow, Cambridge university press, 2009.

[33] T. Müller, A. Sänger, P. Habisreuther, T. Jakobs, D. Trimis, T. Kolb, N. Zarzalis, Simulation of the primary breakup of a high-viscosity liquid jet by a coaxial annular gas flow, Int. J. Multiph. Flow 87 (2016) 212–228.

[34] C. W. Hirt, B. D. Nichols, Volume of fluid (vof) method for the dynamics of free boundaries, J. Comput. Phys. 39 (1) (1981) 201–225.

[35] J. Fröhlich, Large eddy simulation turbulenter Strömungen, Teubner Verlag, Wiesbaden, 2006.

[36] H. Tennekes, J. Lumley, A first course in turbulence, MIT press, 1972.

[37] G. Agbaglah, R. Chiodi, O. Desjardins, Numerical simulation of the initial destabilization of an air-blasted liquid layer, J. Fluid Mech. 812 (2017) 1024–1038.